ScienceAdvances AAAS Manuscript Template

Giant electromechanical coupling of relaxor ferroelectrics controlled by polar-nanoregion vibrations

M. E. Manley,[1,*] D. L. Abernathy,[2] R. Sahul,[3†] D. E. Parshall,[4] J. W. Lynn,[4] A. D. Christianson,[2] P. J. Stonaha,[1] E. D. Specht,[1] J. D. Budai[1]

[1]Materials Science and Technology Division, Oak Ridge National Laboratory, Oak Ridge, Tennessee 37831, USA
[2]Quantum Condensed Matter Division, Oak Ridge National Laboratory, Oak Ridge, Tennessee 37831, USA
[3]TRS Technologies, State College, Pennsylvania 16801, USA
[4]NIST Center for Neutron Research, National Institute of Standards and Technology (NIST), Gaithersburg, Maryland 20899, USA

*Corresponding author. Email: manleyme@ornl.gov
[†]Presently at Meggitt Sensing Systems, Irvine, California 92606, USA

Relaxor-based ferroelectrics are prized for their giant electromechanical coupling and have revolutionized sensor and ultrasound applications. A long-standing challenge for piezoelectric materials has been to understand how these ultrahigh electromechanical responses occur when the polar atomic displacements underlying the response are partially broken into polar nanoregions (PNRs) in relaxor-based ferroelectrics. Given the complex inhomogeneous nanostructure of these materials, it has generally been assumed that this enhanced response must involve complicated interactions. By using neutron scattering measurements of lattice dynamics and local structure, here we show that the *vibrational modes* of the PNRs enable the giant coupling by softening the underlying macro-domain polarization rotations in relaxor-based ferroelectric PMN-*x*PT ((1 − *x*)[Pb ($Mg_{1/3}$ $Nb_{2/3}$)O_3]–*x*$PbTiO_3$) (*x* = 30%). The mechanism involves the collective motion of the PNRs with transverse acoustic phonons and results in two hybrid modes, one softer and one stiffer than the bare acoustic phonon. The softer mode is the origin of the macroscopic shear softening. Furthermore, a PNR mode and a component of the local structure align in an electric field and this enhances the shear softening further, revealing a way to tune the ultrahigh piezoelectric response by engineering the elastic shear softening.

One Sentence Summary: Polar-nanoregion vibrations control the ultrahigh piezoelectric response of relaxor-based ferroelectrics used in applications.

INTRODUCTION

Understanding how inhomogeneous nanoregions enhance functional properties is an outstanding scientific challenge for a broad class of materials that includes relaxor ferroelectrics (*1*), but also superelastic strain glass shape memory alloys (*2*), colossal magnetoresistance manganites, diluted magnetic semiconductors, and some superconductors (*3*). The relaxor-based ferroelectrics PMN-*x*PT ((1 − *x*)[Pb ($Mg_{1/3}$ $Nb_{2/3}$)O_3]–*x*$PbTiO_3$) and PZN-*x*PT ((1 − *x*)[Pb ($Zn_{1/3}$ $Nb_{2/3}$)O_3]–*x*$PbTiO_3$), in particular, have electromechanical responses that are tenfold larger than industry-standard PZT ($PbZrO_3$-$PbTiO_3$) piezoelectric ceramic materials (*1,4*) and have dramatically improved technologies ranging from medical 3D ultrasonography to sonar (*5*). Key features of the parent relaxor ferroelectrics, PMN and PZN, are

inhomogeneous polar nanoregions (PNRs) (*6-9*), which have been invoked to explain their slow dielectric relaxation and diffuse phase transitions (*6-9*). With increasing PT, however, large domains form below the Curie temperature (T_C) (*7*) and the materials behave more like conventional ferroelectrics (e.g. $(Pb(Zr,Ti)O_3$ and $(K,Na)NbO_3$).

A morphotropic phase boundary (MPB) occurs in relaxor-based ferroelectrics, in which the structure changes from rhombohedral to tetragonal (for $x > 9\%$ for PZN-xPT and for $x > 30\%$ for PMN-xPT) (*10*). It is near this phase instability that the largest values for the electromechanical coupling occur (*4, 10-13*). Peaks in the piezoelectric response occur near MPBs and polymorphic phase transitions in conventional ferroelectric materials—and even in a homogeneous ferroelectric with a pressure induced transition (*14*) —but none of these materials have the ultrahigh piezoelectric responses of the relaxor-based ferroelectric crystals, which have longitudinal piezoelectric coefficients $d_{33} > 1500$ pC/N and electromechanical coupling factors $k_{33} \sim 0.9$ (*4*). These findings suggest that relaxor features play an important role (*15*), although a portion of this enhanced response also comes from the fact that the relaxor-based ferroelectrics are single crystals. Xu *et al.* (*16*) found that PNRs are associated with phonon softening and argued that this may underlie the phase instability, but how PNRs soften phonons was not explained.

More recently, it was shown that PNRs form by phonon localization (*17*), and that these localized phonons delocalize below T_C for compositions near the MPB (*17*). Phonon localization means some phonons become trapped in small regions of the crystal, and decouple from the spatially extended phonons. The localized modes have frequencies that are independent of wavevector (dispersionless), indicating that they are stationary (*17*). The underlying mechanism was attributed to Anderson localization (*17*), in which waves become trapped by a constructive interference effect in disorder-scattered waves (*18*). In this picture, the static (or slow) atomic displacements of the PNRs are the average local distortions (local relaxation) associated with phonon localization occurring at much higher frequencies. Anderson localization as a mechanism for PNR formation was also recently deduced from first-principle simulations (*19*) and derived theoretically from equations used to describe relaxor ferroelectric behavior (*20*). An earlier model explained PNRs in terms of intrinsic localized modes (*21-23*), in which nonlinearity is responsible for decoupling the local dynamics from the extended phonons. In this model, decoupling occurs because nonlinearity shifts the frequency of the local vibrations into a gap between modes, where they do not resonate with any of the extended mode (*24*). The observed localization, however, occurs within the phonon bands and with characteristics matching Anderson localization (*17*). In either case, delocalization occurs when these same modes develop dispersion as they couple to and move together with the spatially extended phonons, as hybrid modes.

Here, we demonstrate that the hybridization of the PNR local dynamics with the transverse acoustic (TA) phonons results in a shear softening that enables the giant electromechanical coupling (*25*). The hybridization splits the TA mode into two phonons, one lower frequency (softer) and one higher frequency (stiffer) than the bare acoustic phonon. The stiffer mode exhibits antisymmetric motion, meaning the PNRs move out of phase with the phonon, and it is the restoring force (coupling) between PNRs and the lattice that stiffens this mode. The softer mode exhibits symmetric motion, meaning the PNRs move in phase with the phonon, and this slows the mode down. This behavior is known as anticrossing or sometimes avoided crossing because of the way the hybrid modes appear to avoid each other in phonon dispersion relations (*26*). We also show that aligning the local modes and local structure in an electric field can enhance this phonon softening. In this way, the local vibrations of PNRs exert an

enormous influence over the elastic shear stiffness, and this effect can be used to both understand and predict enhancements in the giant electromechanical response of relaxor-based ferroelectrics.

RESULTS

Neutron scattering on unpoled PMN-PT

The neutron scattering intensity maps in Fig. 1, A and B show the phonon dispersion for unpoled PMN-30%PT above and below the Curie temperature, T_C. These time-of-flight neutron scattering maps show wave vectors along $\boldsymbol{Q}$ = [2+H, -2+H, 0] for 0.0 < H < 0.4, which selects preferentially for transverse phonons polarized along [1, -1, 0] and propagating along [1, 1, 0] (in the rhombohedral state below T_C the coordinates refer to the pseudo-cubic unit cell, which is justified since different domains have zone centers shifted by less than 0.4% owing to the smallness of the lattice distortions (*27*)). On cooling below T_C, the transverse acoustic phonon splits into two branches. The splitting between these branches is about 1.5 meV at H = 0.24 (integrated over H = [0.2, 0.28]), Fig. 1B, right panel. The intensity of the lower branch extends out to about H = 0.24 at an energy of 3 meV (Fig. 1 B). Compared to the TA phonon above T_C (Fig. 1A) the upper branch is 0.6 meV higher at H = 0.3, while the lower branch is about 1 meV lower. Interestingly, the intensity of the lower branch extends out to about the same range as PNR diffuse elastic scattering observed above T_C (*28*, *7*). Figure 1, C and D illustrates the behavior of the PNR diffuse scattering. Above T_C, Fig. 1C, the PNR diffuse scattering forms a lobe of intensity that extends out to about H ~ 0.2 (*7*), while below T_C, Fig. 1D, the diffuse scattering diminishes and the remaining intensity appears closer to the Bragg peak (*7*). This suggests that the PNR diffuse elastic intensity moves into the lattice dynamics on cooling below T_C. To test this idea further, we mapped the intensity of the lower TA phonon branch integrated over 3±1 meV in the (*HK*0) plane, Fig. 1E. As can be seen by comparing Fig. 1E and Fig. 1C (after (*28*, *7*)) the intensity distribution of the lower branch closely resembles the lobe of PNR diffuse scattering above T_C, thus supporting the idea that the PNR diffuse elastic scattering merges with the lattice dynamics. A merging of the PNR diffuse scattering with the lattice dynamics is an expected consequence of coupling the slow PNR dynamics above T_C (*29*) to the lattice below T_C.

The simple model calculation shown in Fig. 2 illustrates how coupling a lattice to small localized clusters representing PNRs (Fig. 2C) results in two TA-PNR hybrid modes (Fig. 2D). Details are provided in Supplementary Materials Calculations. This behavior is a general consequence of coupling modes that share a common frequency and can be understood in terms of an anticrossing (*26*). Consider the two motions for the TA phonon and random PNRs illustrated in Fig. 2E. Without TA-PNR coupling, the PNR motion occurs independently of the bulk-crystal phonon, and hence the frequencies for these two scenarios can be identical. With coupling, the frequencies of these two motions become different. In the antisymmetric mode, the coupling results in a restoring force between the PNR and the TA phonon displacements, which stiffens the collective motion. In the symmetric mode, the cooperative motion of the PNRs with the phonon increases the effective mass of the oscillation, and this lowers the frequency (*26*). The onset of coupling below T_C (Fig. 1) makes sense since the spontaneous polarization of the lattice engages coupling to PNRs through a dipole interaction. This is also consistent with the ~11.5 meV PNR local mode developing dispersion below T_C (*17*), since this dispersion also indicates a coupling to the lattice. Using triple-axis neutron scattering we confirm that dispersion develops in the same way for PNR local modes in PZN-5%PT and PMN-38%PT on cooling below T_C, see Supplementary Materials Fig. S1. The absence of PNR coupling to the lattice above T_C is surprising, but has been explained in terms of an Anderson-type phonon localization mechanism occurring at higher frequencies (*17-20*), in which wave interference from disorder scattering effectively decouples local

regions (*18*). As discussed in the next section, however, there are multiple components to the PNR diffuse scattering, not all of which merge with the lattice dynamics, and the situation must be sorted out by poling the crystals (*30*).

Neutron scattering on poled PMN-30%PT

To explore the effects of poling on the TA-PNR mode hybridization, the ~11.5 meV PNR local mode (*17*), and the PNR diffuse elastic scattering, a PMN-30%PT crystal was electric-field-poled along the [100] direction. The [100]-poling direction is chosen here because the resulting 4R "engineered" domain structure elicits the largest piezoelectric response (*31*) (the "4R" refers to the occurrence of just four of the eight <111>-type rhombohedral domains; i.e. the four domains inclined towards the [100]-poling axis).

Comparing Fig. 1, B and F reveals the effect of [100]-poling on the transverse [110] phonons. Upon poling, the [110]-TA phonon splitting increases from 1.5 meV (Fig. 1B) to 2 meV (Fig. 1F). This 2 meV splitting is also confirmed with an equivalent measurement in the (1,-1,0) zone, Fig. 2G. The lower branch of the split TA mode also appears significantly softened near the zone center in the poled crystal compared to the unpoled crystal; the TA phonon at $H = 0.1$ softens from 3.2 meV to 2.2 meV (see left panels of Fig. 1, B and F). Even closer to the zone center at $H = 0.05$, the [100]-poled crystal has a TA phonon peak that merges with the elastic line and appears four times more intense. The fourfold increase in intensity is consistent with a phonon frequency that is half the value since the scattering intensity of a phonon in the high temperature limit scales as the inverse square of the phonon frequency (*32*). Hence, the TA phonon splitting results in a lower branch that is softer by about a factor of two, and this includes the long-wavelength modes occurring near the zone center ($H = 0$). According to the simple phonon model in Fig. 2, the increased splitting and shear mode softening is consistent with an increase in the effective mass of the PNRs carried by the TA-PNR mode, M_{PNR}. This suggests that poling results in a larger fraction of the PNRs being carried in this TA-PNR mode. As discussed below, it is the softening of this same [110]-TA shear mode that enables the giant electromechanical response.

A direct alignment of the PNR local mode (*17*) polarization with the [100]-poling direction is evidenced in Fig. 3, A and B. Figure 3A shows measurements in a transverse geometry that selects for modes displacing atoms nearly parallel to the [100]-poling direction (see schematic of scattering geometry in Fig. 3). In this direction the PNR mode, between the transverse optic (TO) and TA modes near 11 meV, appears strongly enhanced; relative to the respective TO phonon intensities, the PNR mode is about three times more intense than for the unpoled PMN-30%PT (*17*). There is also a hint of some splitting of the TA phonon in the cut integrated over $-0.5 < K < -0.4$, but this is difficult to resolve and much weaker than that observed along the [110] direction (Fig. 1, B and F). The measurements in Fig. 3B are in a similar transverse geometry, but selects for modes displacing atoms (nearly) perpendicular to the [100]-poling direction. In this direction, the PNR modes are absent, and there is no evidence of splitting in the TA phonon peak. The dispersion in the TO phonon is also steeper without the PNR mode, falling ~2 meV lower near the zone center and not appearing as flat near the zone edge (Fig. 3, A and B). The flattening of the TO phonon in Fig. 3A can be understood as a repulsion between the TO phonon and PNR mode (the flatter mode contributes a sharper and more intense TO peak to the integration cut). Taken together, these results show that the high-frequency PNR modes align with the [100]-poling field and modify the TO phonon along the poling direction.

The PNR diffuse elastic scattering also appears altered parallel to the poling direction (Fig. 3, C and D) relative to equivalent perpendicular directions (Fig. 3, E and F), indicating a rearrangement of static local displacements. The changes in diffuse scattering occur primarily in broad planes oriented perpendicular to the poling direction, while the more complex scattering around the Bragg peaks does not change, as seen in the difference images in Fig. 3, G and H. The broad diffuse intensity integrated over L (inset in Fig. 3H) fits a profile

$$I_{[H,-0.5,0]} - I_{[0.5,-H,0]} = \alpha \times H^2 \cos\left(2\pi H(1/2)\right) + \beta \times H \sin\left(2\pi H(1/2)\right), \quad (1)$$

and a monotonic background, where α and β are constants of the fit. This is a known solution for a crystal with additional well-defined local displacements between atomic pairs separated by $a/2$ in the [100]-poling direction (*33*). The decrease in the monotonic diffuse scattering indicates a corresponding decrease in local displacements occurring with random magnitudes.

There exist two components to the diffuse scattering in relaxor-based ferroelectrics: a butterfly-shaped pattern that appears around Bragg peaks, and the broader component described above. The former has been the focus of the majority of previous studies of the diffuse scattering in relaxor and relaxor-based ferroelectrics (*28, 34-38*). Xu et al. observed the latter in the scattering from [100]-poled PZN-4.5%PT (*39*), but the measurement did not cover enough of reciprocal space to observe the broad modulations across $\boldsymbol{Q}$-space. Pair distribution function analysis on PMN powders indicate local Pb off-centering on this scale (*40*), but these studies did not include poling effects. Measurements of the local mode structure factor at high temperatures also indicate that well-localized modes form first near the Burns temperature and then drive the formation of the larger PNR structures (~ 2 nm) on cooling (*17*), which indicates that both components of the diffuse scattering are associated with the same PNRs. This is also supported by the fact that the poling induced [100] local displacements (Fig. 3) also appear to modify the TA-PNR mode hybridization along the [110] direction (Fig. 1, B and F). Interestingly, the bulk rhombohedral domains do not rotate into the [100] direction, but rather distort along the four <111>-type directions inclined toward the [100] poling direction, in the 4R domain structure (*31*). However, by applying a much larger electric field, it is possible to induce a phase transition to a single tetragonal domain poled along [100] (*1*). Hence, the PNR modes and local displacements are more easily aligned along the [100] poling direction than the ferroelectric domains in which they are embedded, and this is expected since the ferroelectric domains are large, static, and pinned.

DISCUSSION

The observed shear mode softening (Fig. 1) is consistent with ultrasonic pulse echo measurements that show a soft shear acoustic mode along [110] in the (001) plane for [100]-poled PMN-33%PT (*41*) —this is equivalent to the TA phonon in Fig. 1 at long wavelengths ($H \rightarrow 0$). A similar ultrasonic result was found for [100]-poled PZN-4.5%PT (*42*). In these studies, it was argued that the soft shear mode must result from domain motion induced by the ultrasound measurement (*42*). The phonon softening in Fig. 1, B and F, shows, however, that shear softening extends to wavelengths much shorter than the domain size. From the picture presented in Fig. 2E we can understand that the softening originates with the increased effective mass felt by the symmetric mode as more PNRs couple to and move collectively with the TA phonon. A key point here is that the PNRs are smaller than a large share of the phonon

wavelengths, and for this reason they manifest in way that is more akin to an impurity mode (*43*) than to a macroscopic domain.

The TA phonon softening (Fig. 1) is also reminiscent of the softening observed using neutron scattering in [111]-poled single domain PZN-4.5%PT for the same TA mode, it is the phonons which are aligned with PNR diffuse scattering patterns that soften (*16*). In these measurements, however, neither the PNR vibrational modes (*17*) nor the anticrossing of the phonons (Fig. 1) were detected. These features were easily missed because the ~0.3 cm^3 crystal used (*16*) was about sixty times smaller than the ~20 cm^3 crystals used herein (Fig. S2, Supplementary Materials). With this knowledge, we can now understand that the relationship between the PNRs and phonon softening described by Xu *et al.* (*16*) likely originates with a hybridization of the PNRs with TA phonon (Figs. 1 and 2).

The shear softening induced by [100]-poling (Fig. 1F) relates directly to the ease of the polarization rotations (*25*) underlying the giant electromechanical coupling utilized in applications (*4*). The high longitudinal piezoelectric coefficients along the poling axis for the [100]-poled 4R engineered domain (*31*) state is attributed to a high shear piezoelectric response in the single domain state (*4,44-47*). This is because the polarization rotations involve a shearing of the individual domains (*1*). Figure 4 illustrates how the softening of the [110]-TA phonons observed in Fig. 1 implies a softening of these shear deformations. The soft shear mode (Fig. 4A) makes it easy to tilt the [111] axis about [001] (Fig. 4B), whereas an equivalent soft shear makes it easy to tilt about [010] (Fig. 4C). Taken together, the [111] axis is easy to tilt toward the [100] poling axis (Fig. 4D), and the same argument applies to all 4R domains. The result is the large piezoelectric response along the [100]-poling direction (Fig. 4E). The alignment of the PNR modes acts synergistically with the intrinsic effect of being near the MPB to lower the energy barriers of the polarization rotations (*25*), since the MPB occurs even without PNR mode alignment. Interestingly, Pirc *et al.* (*48*) proposed a semi-microscopic model for PNR-enhanced electromechanical coupling, in which the interactions between PNRs are explained in terms of a dipole-phonon interaction. However, the effect coupling the phonons to the PNR vibrations, which underlies the anticrossing induced shear softening, was not considered.

Our results reveal that domain engineering of relaxor-based ferroelectric single crystals (*31*) enhances the electromechanical coupling for two reasons, one deliberate and one serendipitous. While the deliberate 4R arrangement of the domains mechanically facilitates the conversion of the high shear piezoelectric response into a longitudinal response (*31*), the serendipitous alignment of the PNR vibrational modes and local structure (Fig. 3) enhances this shear response further by softening the TA phonon via the anticrossing (Fig. 1F). This engineered phonon softening was likely missed as a contribution in bulk measurements (*4*) because single-domain <111>-poled crystals used for comparison also have TA phonons that are softened by having the PNR modes aligned during the poling process (*16*). The underlying cause is important to recognize, however, since an optimally engineered relaxor-based ferroelectric crystal should enhance both the domain mechanics (*31*) and the appropriate shear softening (*4*) in order to maximize the electromechanical coupling. In this context, it is most interesting that the high-frequency PNR vibrational modes fully align with the [100]-poling field (Fig. 3) while the larger domains remain in the 4R configuration unless much larger fields are applied (*1*). This suggests that it should be possible to engineer the domain structure and the local structure/dynamics independently, optimizing each to improve performance.

Our work establishes the crucial role *nanoregion local vibrations* play in the performance of relaxor-based ferroelectrics, and reveals an elastic softening mechanism that is likely applicable to other nanostructured materials. For example, ferroelastic nanoregions might enable the superelasticity of shape memory strain glass alloys (*2*) by inducing a similar elastic softening. Thus our work provides a new perspective for understanding and controlling the performance of nanostructured materials.

METHODS AND MATERIALS

Time-of-flight inelastic neutron scattering

Time-of-flight measurements were performed on a large (~ 20 cm^3) [100]-poled PMN-30%PT crystal (see Supplementary Materials Fig. S2 for pictures of crystal) and, for comparison, an unpoled PMN-30%PT crystal (~ 10 cm^3) using the Angular-Range Chopper Spectrometer (ARCS) at the Spallation Neutron Source of Oak Ridge National Laboratory (*49*). All measurements where performed with the crystals oriented in the (HK0) plane and with an incident neutron energy of 25 meV. Comprehensive 4-dimensional $\boldsymbol{Q}$-E volumes of data were obtained by rotating the angle between the [100] axis and the incident beam in 0.5 degree steps and combining the data using MSlice in the Data Analysis and Visualization Environment (DAVE) software (*50*). For the unpoled PMN-30%PT crystal data were collected at each angle from 0 to 60 degrees. For the poled PMN-30%PT crystal data were collected at each angle from -70 to 55 degrees to obtain complete data set that includes $\boldsymbol{Q}$ values in directions both perpendicular to and parallel to the [100]-poling direction in the (*HK*0) plane.

Triple-axis inelastic neutron scattering

Large (~10 cm^3) single crystals of PZN-5%PT and PMN-38%PT were measured using triple-axis neutron spectroscopy. The PMN-38%PT crystal was measured on the BT7 spectrometer at the NIST Center for Neutron Research (*51*). The spectrometer was operated with filtered fixed final neutron energy of 13.7 meV (with horizontal collimation 120': 50': 50': 120' (*32*)) and the crystals were mounted in a furnace with the (*HK*0) reflections in the scattering plane using a vanadium holder (vanadium is used because it scatters incoherently). Measurements were made along [2, K, 0] at 21 equally spaced values of K between 0 and 0.5 at temperatures above and below the Curie temperature (T_C): 515 K and 300 K for PMN-38%PT (T_C = 465 K). The PZN-5%PT crystal, also mounted in a vanadium holder, was measured on the HB3 spectrometer at the High Flux Isotope Reactor at Oak Ridge National Laboratory. The HB3 spectrometer was operated with filtered fixed final neutron energy of 14.7 meV (with horizontal collimation 48': 60': 80': 120') and measurements were made with the same crystal orientation and at the same points in reciprocal space as with BT7, again at temperatures above and below T_C: 500 K and 300 K (T_C = 425 K for PZN-5%PT). Both instruments used pyrolitic graphite PG(002) for the monochromator and analyzer.

Crystal growth and electric field poling

PMN-PT single-crystal boules were grown using a modified Bridgman growth method. The boules were oriented for the major crystallographic orientations $[001]_c$, $[011]_c$, and $[111]_c$ using a Laue X-ray and X-ray diffractometry. Sections of crystals 0.5 cm thick were sliced from the boule using an ID-saw. The composition of the crystals were first estimated from the positions in the crystal boules and then later confirmed by measuring the transition temperatures using high-temperature x-ray diffraction on the individual crystals and comparing these to the known phase diagrams. For the unpoled PMN-30%PT crystals the slices were used as cut.

For poling purposes, two 0.5 cm thick, ~5 cm diameter, slices were cleaned and metallized with ~500 Å layer of chromium and 2000 Å layer of gold using a sputtering process (Fig. S2, Supplementary Materials). The metallized section was then poled using a polarization bath. The crystal slice is immersed in a bath of fluorinert oil (silicone oil with a high dielectric strength) and a DC electric field is applied. For the rhombohedral PMN-30%PT crystal, the crystal samples were poled by application of a DC electric field of 4 kV cm^{-1} at room temperature. Piezoelectric charge coefficient (d_{33}) was measured using a d_{33} meter to determine if the crystal slices were poled into a piezoelectric state. After poling, polarization changes as the function of applied electric field were observed on batch qualification samples using a hysteresis loop device that works based on a Sawyer-Tower circuit. This measurement uses an integrator to determine the charge per unit area formed on the electroded surface of a dielectric subjected to an electric field. The voltage is applied in the form of a biased (unipolar) triangle wave (0 to peak) for a small number of cycles (~3). The hysteresis area between the field ascending and field descending portions of the curve is proportional to the energy lost as heat during a charge-discharge cycle and this hysteresis loop represents characteristic behavior that is typical of ferroelectric materials.

SUPPLEMENTARY MATERIALS

Supplementary Calculations
Fig. S1. Phonon dispersion curves measured along $\boldsymbol{Q}$ = [2,K,0] in PZN-5%PT and PMN-38%PT, both above and below T_C.
Fig. S2. Photograph of poled PMN-30%PT crystals.

REFERENCES AND NOTES

1. S.-E. Park, T. R. Shrout, Ultrahigh strain and piezoelectric behavior in relaxor based ferroelectric single crystals. *J. Appl. Phys.* **82**, 1804 (1997).

2. Y. Wang, X. Ren, and K. Otsuka, Shape memory effect and superelasticity in a strain glass alloy. *Phys. Rev. Lett.* **97**, 225703 (2006).

3. E. Dagotto, Complexity in strongly correlated electronic systems. *Science* **309**, 257 (2005).

4. S. Zhang, and F. Li, High performance ferroelectric relaxor-$PbTiO_3$ single crystals: Status and perspective. *J. Appl. Phys.* **111**, 031301 (2012).

5. K. Uchino, *Piezoelectric Actuators and Ultrasonic Motors* (Kluwer Academic, 1996).

6. G. Burns, and F. H. Dacol, Crystalline ferroelectrics with glassy polarization behavior. *Phys. Rev. B* **28**, 2527–2530 (1983).

7. M. Matsuura, K. Hirota, P. M. Gehring, Z.-G. Ye, W. Chen, and G. Shirane, Composition dependence of the diffuse scattering in the relaxor ferroelectric compound (1-x)$Pb(Mg_{1/3}Nb_{2/3})O_3$-x$PbTiO_3$ (0<x<0.4). *Phys. Rev. B* **74**, 144107 (2006).

8. R. Blinc, V. Laguta, and B. Zalar, Field cooled and zero field cooled ^{207}Pb NMR and the local structure of relaxor $PbMg_{1/3}Nb_{2/3}O_3$. *Phys. Rev. Lett.* **91**, 247601 (2003).

9. V. V. Shvartsman, and A. L. Kholkin, Domain structure of 0.8$Pb(Mg_{1/3}Nb_{2/3})$-0.2$PbTiO_3$ studied by piezoresponse force microscopy. *Phys. Rev. B* **69**, 014102 (2004).

10. Y. Guo, H. Luo, D. Ling, H. Xu, T. He, and Z. Yin, The phase transition sequence and the location of the mophotropic phase boundary region in $(1 - x)[Pb(Mg_{1/3}Nb_{2/3})O_3]$–$xPbTiO_3$ single crystal. *J. Phys.: Condens. Matter* **15** No 2 L77-L82 (2003).

11. Tian, P. D. Han, and D. A. Payne, Measurements along the growth direction of PMN-PT crystals: dielectric, piezoelectric, and elastic properties. *IEEE Trans. Ultrason. Ferroelectr. Freq. Control* **54**, 1895 (2007).

12. F. Li, S. Zhang, Z. Xu, X. Wei, J. Luo, and T. R. Shrout, Composition and phase dependence of the intrinsic and extrinsic piezoelectric activity of domain engineered (1-x)Pb(Mg1/3Nm2/3)O3-xPbTiO3 crystals. *J. Appl. Phys.* **108**, 034106 (2010).

13. Z. Kutnjak, J. Petzelt, and R. Blinc, The giant electromechanical response of ferroelectric relaxors as a critical phenomena. *Nature* **441**, 956-959 (2006).

14. M. Ahart, M. Somayazulu, R. E. Cohen, P. Ganesh, P. Dera, H. Mao, R. J. Hemley, Y. Ren, P. Liermann, and Z. Wu, Origin of morphotropic phase boundaries in ferroelectrics. *Nature* **451**, 545-548 (2008).

15. D. Phelan, C. Stock, J. A. Rodriguez-Rivera, S. Chi, J. Leao, X. Long, Y. Xie, A. A. Bokov, Z.-G. Ye, P. Ganesh, and P. M. Gehring, Role of random electric fields in relaxors. *Proc. Natl. Acad. Sci.* **111**, 1754 (2014).

16. G. Xu, J. Wen, C. Stock, and P. M. Gehring, Phase instability induced by polar nanoregions in a relaxor ferroelectric system. *Nat. Mater.* **7**, 562–566 (2008).

17. M. E. Manley, J. W. Lynn, D. L. Abernathy, E. D. Specht, O. Delaire, A. R. Bishop, R. Sahul, and J. D. Budai, Phonon localization drives polar nanoregions in a relaxor ferroelectric. *Nat. Commun.* **5**:3683 doi: 10.1038/ncomms4683 (2014).

18. A. Lagendijk, B. van Tiggelen, and D. S. Wiersma, Fifty years of Anderson localization. *Phys. Today* **62**, 24–29 (2009).

19. A. R. Akbarzadeh, S. Prosandeev, E. J. Walter, A. Al-Barakaty, and L. Bellaiche, Finite-temperature properties of $Ba(Zr, Ti)O_3$ relaxors from first principles. *Phys. Rev. Lett.* **108**, 257601 (2012).

20. D. Sherrington, BZT: a soft pseudospin glass. *Phys. Rev. Lett.* **111**, 227601 (2013).

21. A. Bussmann-Holder, A. R. Bishop, and T. Egami, Relaxor ferroelectrics and intrinsic inhomogeneity. *Europhys. Lett.* **71**, 249–255 (2005).

22. A. R. Bishop, A. Bussmann-Holder, S. Kamba, and M. Maglione, Common characteristics of displacive and relaxor ferroelectrics. *Phys. Rev. B* **81**, 064106 (2010).

23. J. Macutkevic, J. Banys, A. Bussmann-Holder, and A. R. Bishop, Origin of polar nanoregions in relaxor ferroelectrics: nonlinearity, discrete breather formation, and charge transfer. *Phys. Rev. B* **83**, 184301 (2011).

24. D. K. Campbell, S. Flach, and Y. S. Kivshar, Localizing energy through nonlinearity and discreteness. *Phys. Today* **57**, 43 (2004).

25. H. Fu, and R. E. Cohen, Polarization rotation mechanism for ultrahigh electromechanical response in single-crystal piezoelectrics. *Nature* **403**, 281-283 (2000).

26. B. Skinner, *There's nothing particularly "spooky" about avoided crossing,* https://gravityandlevity.wordpress.com/2014/04/08/avoided-crossing/, accessed, May, (2016).

27. B. Noheda, Structure and high-piezoelectricity in lead oxide solid solutions. *Curr. Opin. Solid State Mater. Sci.* **6**, 27 (2002).

28. G. Xu, Z. Zhong, H. Hiraka, and G. Shirane, Three-dimensional mapping of diffuse scattering in $Pb(Zn_{1/3}Nb_{2/3})O_3$-x$PbTiO_3$. *Phys. Rev. B* **70**, 174109 (2004).

29. H. Hiraka, S.-H. Lee, P. M. Gehring, G. Xu, and G. Shirane, Cold neutron study on the diffuse scattering and phonon excitations in the relaxor $Pb(Mg_{1/3}Nb_{2/3})O_3$. *Phys. Rev. B* **70**, 184105 (2004).

30. G. Xu, Z. Zhong, Y. Bing, Z.-G. Ye, and G. Shirane, Electric-field-induced redistribution of polar nano-regions in a relaxor ferroelectric. *Nat. Mater.* **5**, 134 (2006).

31. M. Davis, D. Damjanovic, D. Hayem, and N. Setter, Domain engineering of the transverse piezoelectric coefficient in perovskite ferroelectrics. *J. Appl. Phys.* **98**, 014102 (2005).

32. G. Shirane, S. M. Shapiro, J. M. Tranquada, *Neutron scattering with a triple-axis spectrometer: basic techniques* (Cambridge University Press, Cambridge, UK, 2002) p. 28.

33. J. M. Cowley, *Diffraction Physics* (North-Holland Physics, Amsterdam, Netherlands, 1975) p. 260.

34. A. Cervellino, S. N. Gvasaliya, O. Zaharko, B. Roessli, G. M. Rotaru, R. A. Cowley, S. G. Lushnikov, T. A. Shaplygina, and M. T. Fernandez-Diaz, Diffuse scattering from the lead-based relaxor ferroelectric $PbMg_{1/3}Ta_{2/3}O_3$. *J. Appl. Cryst.* **44**, 603 (2011).

35. T. R. Welberry, D. J. Goossens, and M. J. Gutmann, Chemical origin of nanoscale polar domains in $PbZn_{1/3}Nb_{2/3}O_3$. *Phys. Rev. B* **74**, 224108 (2006).

36. M. Pasciak, M. Wocyrz, and A. Pietraszko, Interpretation of the diffuse scattering in Pb-based relaxor ferroelectrics in terms of three-dimensional nanodomains of the 110-directed relative interdomain atomic shifts. *Phys. Rev. B* **76**, 014117 (2007).

37. P. Ganesh, E. Cockayne, M. Ahart, R. E. Cohen, B. Burton, R. J. Hemley, Y. Ren, W. Yang, and Z.-G. Ye, Origin of diffuse scattering in relaxor ferroelectrics, *Phys. Rev. B* **81**, 144102 (2010).

38. A. Bosak, D. Chernyshov, S. Vakhrushev, and M. Krisch, Diffuse scattering in relaxor ferroelectrics: True three-dimensional mapping, experimental artifacts and modeling. *Acta. Crystallogr. A* **68**, 117 (2012).

39. Z. Xu, J. Wen, G. Xu, C. Stock, J. S. Gardner, and P. M. Gehring, Two-component model of the neutron diffuse scattering in the relaxor ferroelectric PZN-4.5%PT. *Phys. Rev. B* **82**, 134124 (2010).

40. T. Egami and S. J. L. Billinge, *Underneath the Bragg Peaks Structural Analysis of Complex Materials* Ed. R. W. Cahn (Pergamon Materials Series, 2003) p. 343.

41. R. Zhang, B. Jiang, and W. W. Cao, Elastic, piezoelectric, and dielectric properties of multidomain $0.67Pb(Mg_{1/3}Nb_{2/3})O_3$–$0.33PbTiO_3$ single crystals. *J. Appl. Phys.* **90**, 3471 (2001).

42. J. H. Yin, B. Jiang, and W. W. Cao, Elastic, piezoelectric, and dielectric properties of $0.955Pb(Zn_{1/3}Nb_{2/3})O_3$–$0.045PbTiO_3$ single crystal with designed multidomains. *IEEE Trans. Ultrason. Ferroelect. Freq. Contr.* **47**, 285 (2000).

43. O. Delaire, I. I. Al-Qasir, A. F. May, C. W. Li, B. C. Sales, J. L. Niedziela, J. Ma, M. Matsuda, D. L. Abernathy, and T. Berlijn, Heavy-impurity resonance, hybridization, and phonon spectral functions in $Fe_{1-x}M_xSi$ (M = Ir, Os). *Phys. Rev. B* **91**, 094307 (2015).

44. L. Bellaiche, A. García, and D. Vanderbilt, Electric-field induced polarization paths in $Pb(Zr_{1-x}Ti_x)O_3$ alloys. *Phys. Rev. B* **64**, 060103 (2001).

45. M. Davis, M. Budimir, D. Damjanovic, and N. Setter, Rotator and extender ferroelectrics: Importance of the shear coefficient to the piezoelectric properties of domain-engineered crystals and ceramics. *J. Appl. Phys.* **101**, 054112 (2007).

46. D. Damjanovic, Comments on origins of enhanced piezoelectric properties in ferroelectrics. *IEEE Trans. Ultrason. Ferroelectr. Freq. Control* **56**, 1574 (2009).

47. E. Sun, and W. Cao, Relaxor-based ferroelectric single crystals: Growth, domain engineering, characterization and applications. *Prog. in Mater. Sci.* **65** 124 (2014).

48. R. Pirc, R. Blinc, and V. S. Vikhnin, Effect of polar nanoregions on giant electrostriction and piezoelectricity in relaxor ferroelectrics. *Phys. Rev. B* **69**, 212105 (2004).

49. D. L. Abernathy, M. B. Stone, M. J. Loguillo, M. S. Lucas, O. Delaire, X. Tang, J. Y.Y. Lin, and B. Fultz, Design and operation of the wide angular-range chopper spectrometer ARCS at the Spallation Neutron Source. *Rev. of Sci. Instr.* **83**, 15114 (2012).

50. R. T. Azuah, L. R. Kneller, Y. Qiu, P.W.W. Tegenna-Piggott, C.M. Brown, J.R.D. Copley, and R.M. Dimeo, DAVE: A Comprehensive Software Suite for the Reduction, Visualization, and Analysis of Low Energy Neutron Spectroscopic Data. *J. Res. Natl. Inst. Stan. Technol.* **114**, 341 (2009).

51. J. W. Lynn, Y. Chen, S. Chang, Y. Zhao, S. Chi, W. Ratcliff, B. G. Ueland, and R. W. Erwin, Double Focusing Thermal Triple Axis Spectrometer at the NCNR. *J. Research NIST* **117**, 61 (2012).

52. C. Kittel, *Introduction to Solid State Physics 7th edition* (John Wiley & Sons, Inc.,1996).

53. A. A. Maradudin, E. W. Montroll, and G. H. Weiss, *Theory of lattice dynamics in the harmonic approximation* (Academic Press, 1963).

ACKNOWLEDGEMENTS

MEM acknowledges useful communications with P. M. Gehring. **Funding:** Research sponsored by the U.S. Department of Energy, Office of Basic Energy Sciences, Materials Sciences and Engineering Division. The portions of this research performed at the Oak Ridge National Laboratory's Spallation Neutron Source and High Flux Isotope Reactor facilities were sponsored by the U. S. Department of Energy, Office of Basic Energy Sciences. We acknowledge the support of the National Institute of Standards and Technology, U.S. Department of Commerce, in providing neutron research facilities used in this work. The identification of any commercial product or trade name does not imply endorsement or recommendation by the National Institute of Standards and Technology. **Author contributions:** M.E.M. conceived of the experiments. D.L.A., M.E.M., J.D.B., and P.J.S. performed the time-of-flight neutron scattering measurements. M.E.M., D.E.P., J.W.L., and A.D.C. performed triple-axis neutron scattering measurements. M.E.M. analyzed all neutron scattering data. E.D.S. performed the x-ray characterization of the single crystal. R.S. grew the single crystals and performed the electric field poling of the single crystals. M.E.M. wrote the manuscript with input from all authors. **Competing interests:** The authors declare that they have no competing interests. **Data and materials availability:** All data that are needed to evaluate the conclusions are included in the paper or supplementary materials. Additional data related to this paper may be requested from manleyme@ornl.gov.

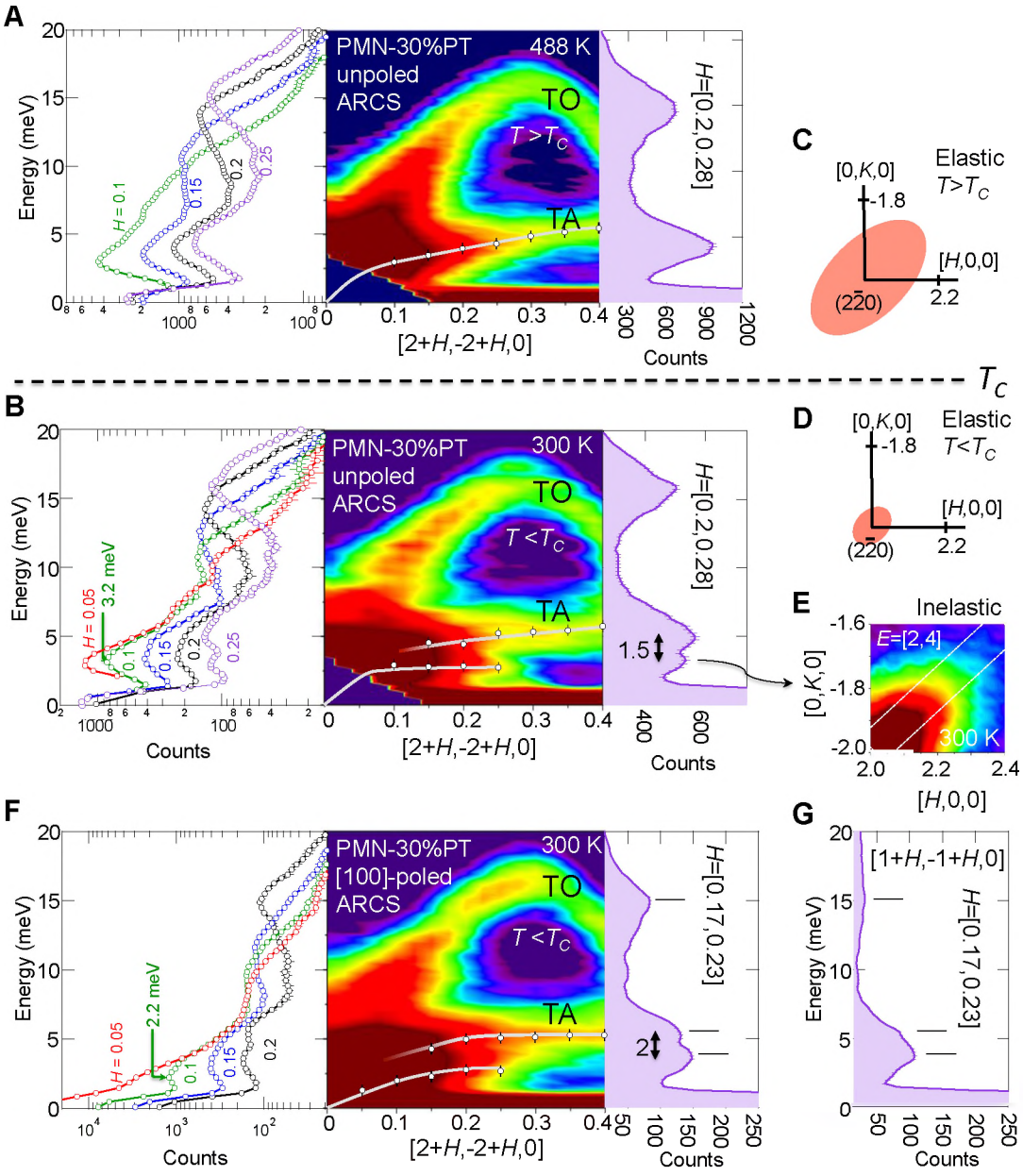

Fig. 1. Phonon dispersion along Q = [2+H, -2+H, 0] (L = 0±0.05) in PMN-30%PT comparing temperature and poling effects. (**A**) Unpoled crystal measured above T_C at 488 K shows a single TA mode. (**B**) Unpoled crystal measured below T_C at 300 K shows a splitting of the TA phonon. (**C**), (**D**) Sketches of the diffuse elastic scattering around (*HH*0) reflections in the (*HK*0) plane, above and below T_C (*7, 28*). (**E**) Inelastic scattering intensity map at the energy of the lower branch of the split TA phonon (E = [2,4] meV) near the (2,-2,0) reflection in the (*HK*0) plane. (**F**) [100]-poled PMN-30%PT shows a dramatic softening of the lower section of the TA branch (left panels) and an increase in the splitting of the TA mode from 1.5 meV to 2 meV (right panels). Data points overlaying the images of the TA phonon (center panels in (**A**) (**B**) and (**F**)) are peak positions from fits to the data and the white lines running through these points are guides to the eye. (**G**) Confirmation of features in the (1,-1,0) zone for same direction, Q = [1+H, -1+H, 0]. The TO and upper TA branch appear relatively weaker in the (1,-1,0) zone, but the same features appear. All measurements were made on the ARCS time-of-flight spectrometer at the Spallation Neutron Source, Oak Ridge National Laboratory.

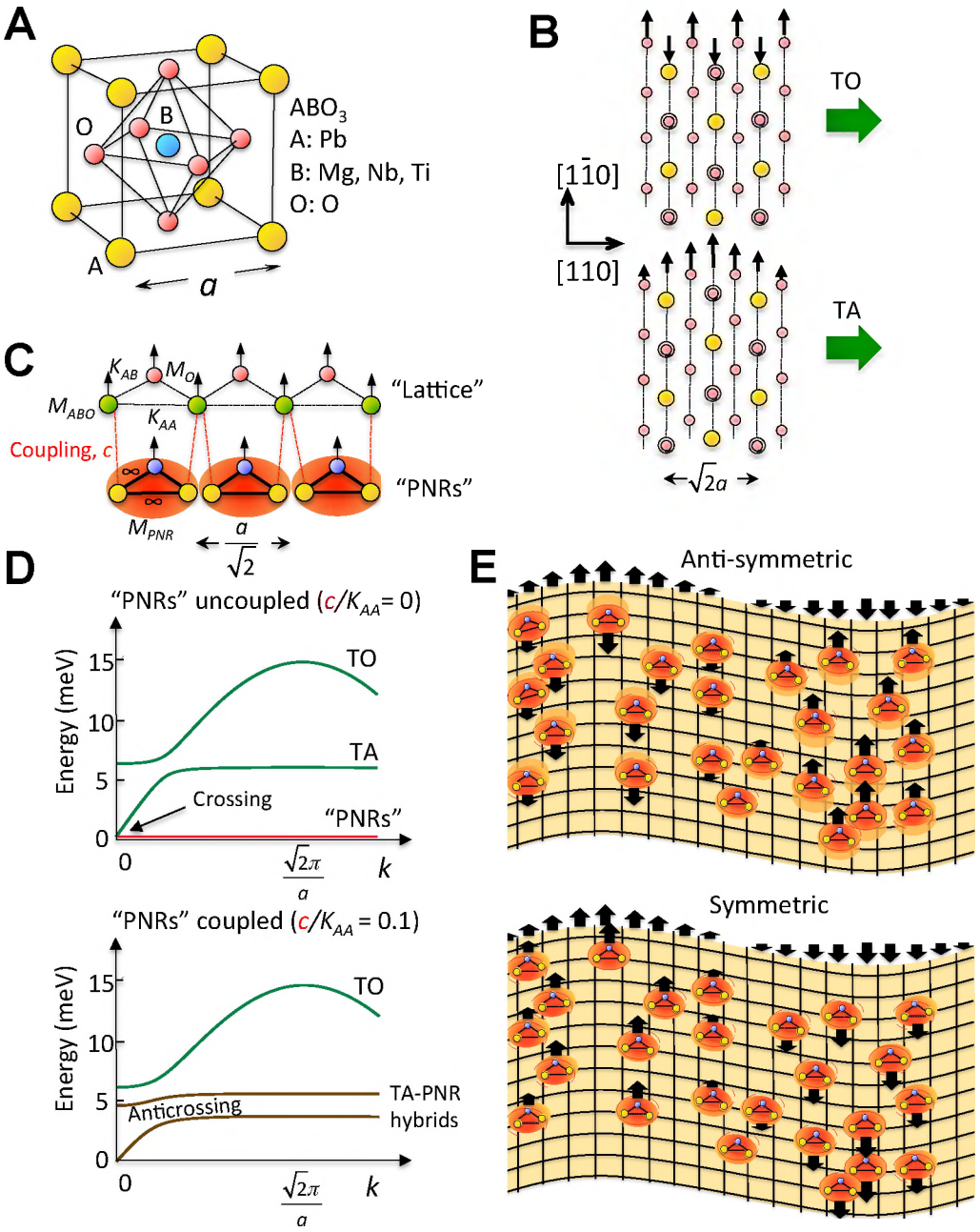

Fig. 2. Simple model for coupling lattice modes to polar nanoregions (PNRs). (**A**) Average crystal structure of PMN-PT. (**B**) The TO and TA phonons are approximated as one-dimension displacements of planes of atoms. (**C**) Model for coupling "PNR" clusters to the lattice, where M_O is the atomic mass of 2O, 32 u, M_{ABO} is the average mass on the alternate plane containing 1A, 1B, and 1O atoms, 286.4 u, and M_{PNR} is the fractional mass of the PNR clusters, 200 u (see Supplementary Materials Calculations). The force constants: K_{AA} = 14,000 u-meV^2, K_{AO} = 500 u-meV^2. The PNRs are assumed to be internally rigid and c accounts for the coupling between the lattice and PNRs. (**D**) The solution for zero coupling, $c/K_{AA} = 0$, exhibits TO and TA modes, and zero-energy PNR cluster dynamics that cross the TA mode at $k = 0$. Solution with coupling, $c/K_{AA} = 0.1$, exhibits an anticrossing with the low-energy dynamics. At $k = 0$ the lower *symmetric* branch has "PNRs" moving in phase and the upper *antisymmetric* branch has them moving out of phase with the lattice. (**E**) Sketch of the symmetric and antisymmetric TA-PNR motions in a lattice partially occupied with PNRs.

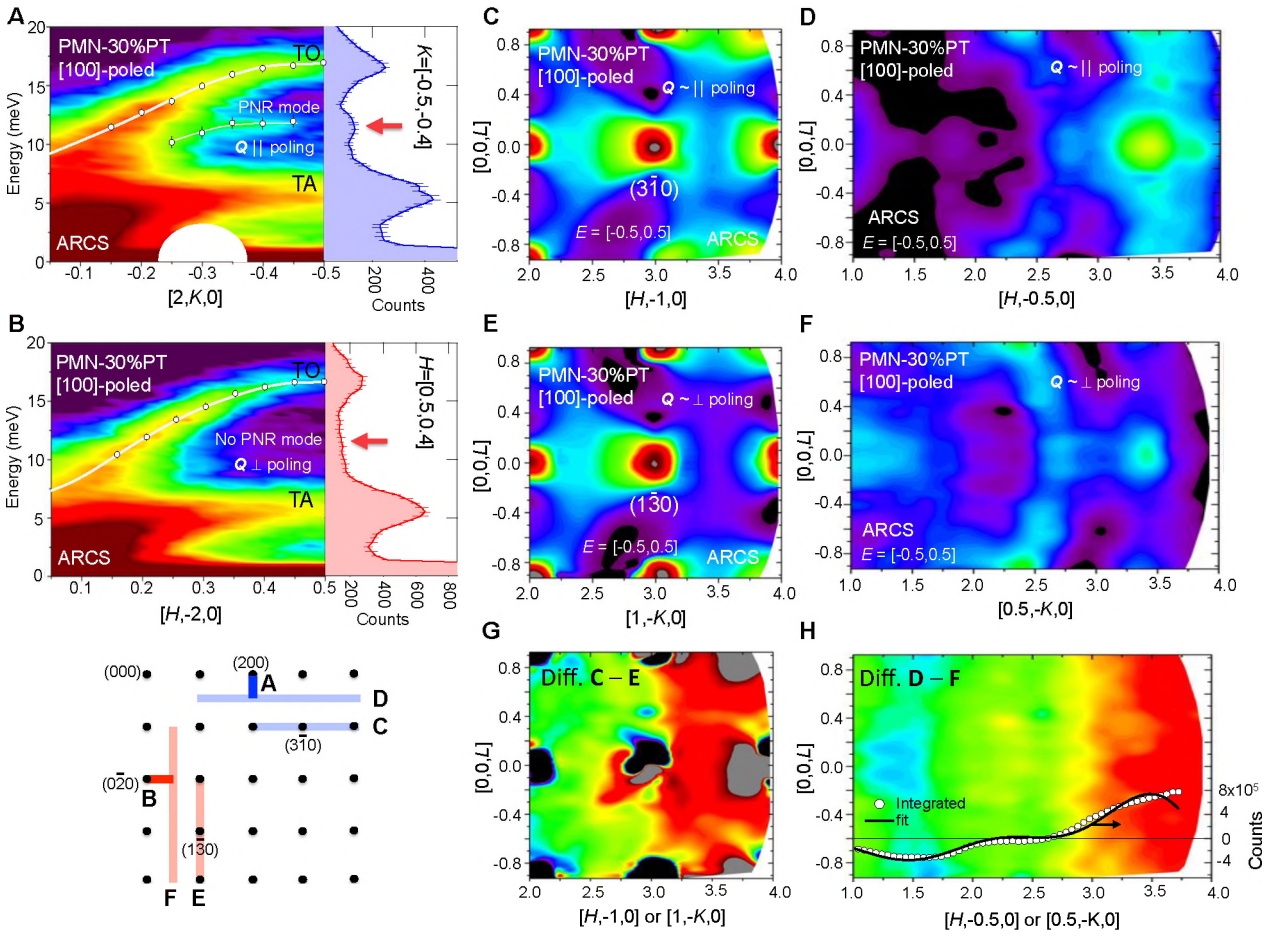

Fig. 3. Time-of-flight neutron scattering measurements of [100]-poled and unpoled PMN-30%PT at 300 K. (**A**) Phonon dispersion measured along $\boldsymbol{Q}$ = [2, K, 0] (H = 2±0.025 and L = 0±0.025). The PNR mode appears enhanced in this direction. (**B**) Phonon dispersion measured along $\boldsymbol{Q}$ = [H, -2, 0] (K = -2±0.025 and L = 0±0.025). The PNR mode does not appear in this direction. The data points overlaying the images in in the left panels of (**A**) and (**B**) are from peak fits and the white lines running through these points are guides to the eye. (**C**), (**D**) Diffuse elastic scattering (E = 0±0.5 meV) measured with $\boldsymbol{Q}$ ~ parallel to the [100]-poling direction on the (H, -1±0.025, L) and (H, -0.5±0.025, L) planes. (**E**), (**F**) Diffuse elastic scattering on the (1±0.025, K, L) and (0.5±0.025, K, L) scattering planes, which are the equivalent to (**C**) and (**D**) except along directions ~ perpendicular to the [100]-poling direction (see diagram for geometries). (**G**), (**H**) Difference images created by subtracting the (**E**) from (**C**) and (**F**) from (**D**), reveals vertical bands of diffuse scattering. The inset data points in (**H**) were obtained by integrating the difference image over L = [-1, 1]. The fit is described in the text. All measurements were made on the ARCS time-of-flight spectrometer at the Spallation Neutron Source, Oak Ridge National Laboratory.

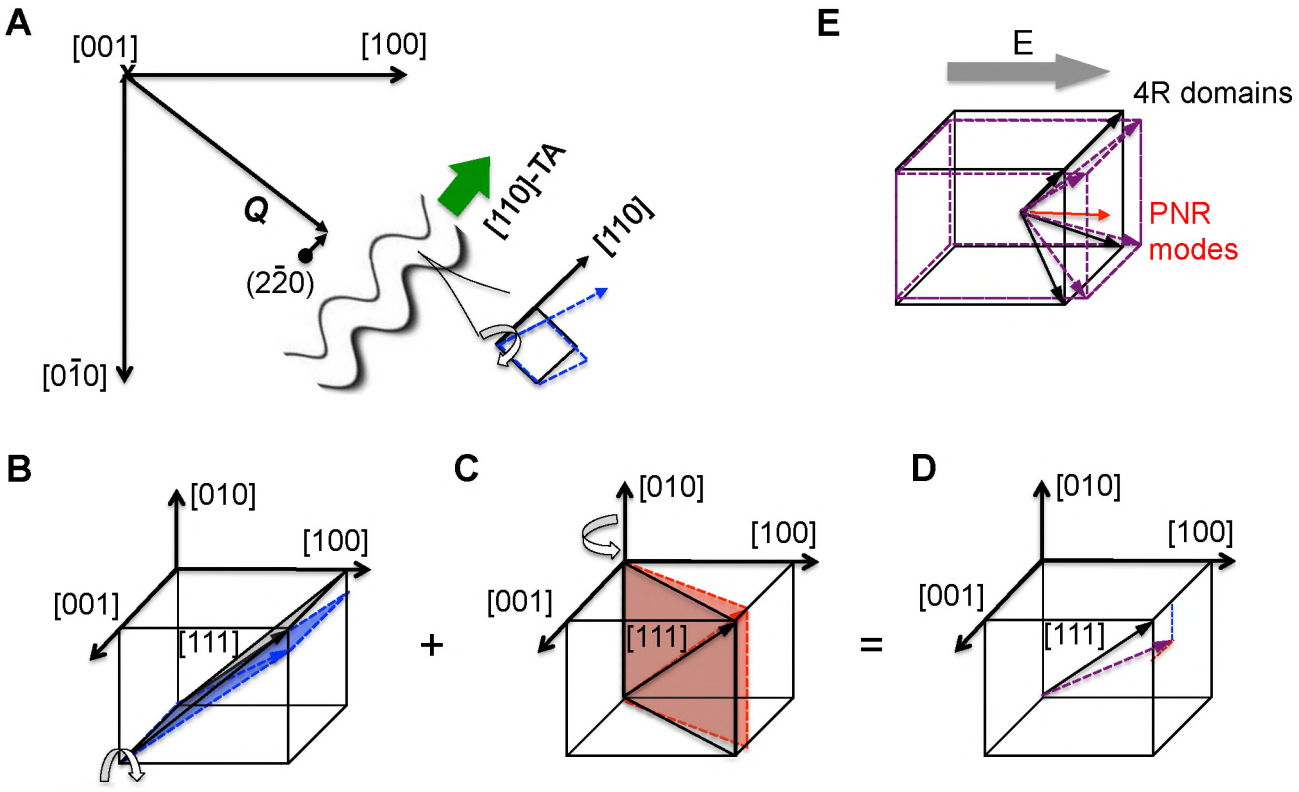

Fig. 4. Relationship between the soft [110]-TA phonon and the giant electromechanical coupling. (**A**) The [110]-TA phonon displacements include a shear deformation that tilts the [110] axis around the non-polar [001] axis. The softening of this phonon at long wavelengths (near the zone center in Fig. 1) implies a softening of the indicated shear distortion. (**B**) The tilting of the [110] axis around [001] also results in the tilting of the [111] axis around [001] since it is in the same tilting plane (the (1, -1, 0) plane). (**C**) An equivalent soft TA phonon involving a tilting of the [111] axis around [010] (the other non-polar axis) must also exist by symmetry. (**D**) Combination of the soft distortions in (**B**) and (**C**) rotates the [111] axis toward the [100] polar axis. (**E**) Equivalent distortions in all four rhombohedral domain variants (4R) (*31*) distort the domains towards the [100]-poling direction under the application of an electric field, E. The [100]-poling aligns the PNR modes along the poling direction (red arrow).